*Am J Physiol Heart Circ Physiol* 330: H388–H403, 2026.
*First published December 24, 2025; doi:10.1152/ajpheart.00759.2025*

american physiological society

AMERICAN JOURNAL OF PHYSIOLOGY
HEART AND CIRCULATORY PHYSIOLOGY

RESEARCH ARTICLE

*Vascular Biology and Microcirculation*

# The "useful" hindrance to flow: quantification of intraluminal valves effect on lymph flow driven by intrinsic mechanism in the diaphragmatic lymphatic network

**Eleonora Solari, Cristiana Marcozzi, Daniela Negrini, and Andrea Moriondo**
*Department of Medicine and Technological Innovation, University of Insubria, Varese, Italy*

## Abstract

The present study investigates the impact of intraluminal valves on lymph transport in rat diaphragmatic collecting vessels, with the aim of clarifying their role in intrinsically driven lymph flow. Using ex vivo fluorescent microsphere tracking and micropuncture techniques, lymph flow, pressure gradients, and hydraulic resistance were quantified in valved and nonvalved segments. Key findings revealed that valves significantly increased lymph velocity (approximately 1,617 μm/s) through their narrower functional section (∼14.4% of vessel cross section) compared with nonvalved segments (∼210 μm/s). The presence of valves required higher pressure gradients (4.15 ± 0.57 cm$H_2O$ vs. 2.16 ± 0.27 cm$H_2O$ in nonvalved segments) but markedly increased net lymph flow (68.0 ± 4.2% vs. 45.7 ± 3.7% of forward flow across valved and nonvalved tracts, respectively) by limiting reverse movement even if biased toward an open state. Despite increasing hydraulic resistance, lymph flow remained laminar, and valves optimized net lymph progression, particularly in larger vessels, where the ratio of net flow to forward flow was independent of vessel size. These results quantify and highlight the pivotal role of intraluminal valves in facilitating efficient, unidirectional net lymph transport, even under low-pressure, oscillatory flow conditions, by adapting to the unique hydraulic properties of the diaphragmatic lymphatic network.

**NEW & NOTEWORTHY** This work quantifies the effect that intraluminal valves exert onto the intrinsic lymph flow in an ex vivo preparation of rat diaphragm. By means of particle tracking analysis and intraluminal hydraulic pressure measurements, the added pressure gradient due to the valve, its functional section and the positive effect on net lymph flow have been carefully measured in a quasiphysiological state, revealing that the open-biased state of the valve is the key to net lymph progression.

*intraluminal valve; intrinsic mechanism; lymphatic vessel; rat diaphragm*

## INTRODUCTION

The lymphatic system plays a pivotal role in maintaining tissue fluid balance and regulating immune responses. It drains extravasated fluid, proteins, and macromolecules (i.e., lymph) from interstitial tissues and serosal cavities, returning them to the blood vascular system; absorbs dietary lipids; and transports immune cells and antigens to lymph nodes, where lymph is filtered and adaptive immune responses are initiated (1–3). The lymphatic network is composed of lymphatic capillaries, which drain lymph and collecting vessels equipped with lymphatic muscle cells (LMCs) and intraluminal secondary valves. These valves segment the vessel into functional units called "lymphangions," which act as short-distance pumps aligned in series, both crucial for proper lymph propulsion. Dysfunctions of lymphatic vessels severely impair lymph transport and reduce lymphatic pumping and flow, leading to lymphedema-related pathologies (4–10).

Lymph formation and propulsion are driven by pressure gradients arising between the interstitial space surrounding capillary vessels and those between adjacent lymphangions. These gradients are attained by a combination of intrinsic and extrinsic mechanisms, affecting transmural and intraluminal hydraulic pressure gradients. The intrinsic mechanism relies on rhythmic, spontaneous contractions of LMCs in the wall of collecting vessels. Lymphangions display cyclical spontaneous contractions, which propagate along the vessel in either the orthograde or retrograde direction, giving rise to oscillatory lymph flow. These contractions originate in pacemaker sites, presumably located in LMCs, displaying spontaneous transient depolarizations (STDs) and/or $I_f$-like currents through hyperpolarization-activated cyclic nucleotide–gated (HCN) channels, which lead to the generation of

Correspondence: A. Moriondo (andrea.moriondo@uninsubria.it).
Submitted 26 September 2025 / Revised 27 October 2025 / Accepted 16 December 2025

action potentials and trigger vessel constrictions (11–15). Spontaneous lymphatic contractility is highly sensitive to chemical and physical changes in the surrounding interstitial tissue, such as local tissue temperature, fluid osmolarity, and transmural pressure gradients, and can be modulated by activation of the autonomic nervous system (16–25). The extrinsic mechanism includes external forces arising in surrounding tissues, such as skeletal muscle contractions, respiratory movements, cardiogenic activity, and intestinal peristalsis. These forces are transmitted to the vessel wall through components of the extracellular matrix (ECM), including anchoring filaments, elastic fibers, and collagen. Collagen is the main ECM component in the interstitial space and plays a dominant role in providing the structural framework (26–28). The intrinsic mechanism is essential for lymph flow in most lymphatics located in soft tissues, whereas the extrinsic one predominates in lymphatics found in body areas undergoing rhythmic tissue displacements. However, they can cooperate within the same anatomical region to optimize lymph flow, as in the diaphragmatic lymphatic network. This network mainly consists of complex peripheral and interconnected lymphatic loops that merge toward the center of the diaphragm into linear vessels arranged longitudinally and/or perpendicularly to the orientation of skeletal muscle fibers (3, 29).

Intraluminal lymphatic valves enable efficient lymph propulsion by minimizing reverse flow through leaflet opening and closing, thereby stepwise overcoming the opposing pressure gradient from one lymphangion to the next (30). They are mainly bicuspid, consisting of two layers of lymphatic endothelial cells (LECs) supported by a connective tissue core. The valve leaflets are firmly attached to the vessel wall and form a funnel-shaped structure that significantly narrows the vessel lumen, providing the only pathway for lymph to advance. In the valve region, LMCs are generally sparse and not functionally well organized for lymphatic contraction (4, 31). In a lymphangion chain, the upstream valve typically closes, whereas the downstream valve opens, resulting in stepwise net forward lymph flow, although some reverse flow is subsequently allowed. Changes in hydraulic pressure ($P_{lymph}$) both upstream and downstream of the valve determine leaflet deflection. An increase in $P_{lymph}$ upstream of a closed valve forces the leaflets to open. Conversely, when $P_{lymph}$ increases at the outflow side and decreases at the inflow side, the leaflets move toward the center of the vessel and the valve closes (Fig. 1, *A* and *B*) (32). Although intraluminal valves were traditionally thought to gate passively based on instantaneous transvalve hydraulic pressure gradients ($\Delta P_{lymph}$), recent studies have revealed a more complex mechanism. The $\Delta P_{lymph}$ required for valve opening and/or closing varies significantly with vessel distention. In mesenteric lymphatics, $\Delta P_{lymph}$ required for intraluminal valve closure increases more than 20-fold (from 0.1 to 2.2 cmH$_2$O) as lymphatics progressively distend, depending on leaflet tension, with valves able to withstand retrograde pressures up to 27 cmH$_2$O. Valve reopening also depends on leaflet distention and transmural pressure. The functional behavior of valves also exhibits distinct dynamics, as opening is generally faster than closing (30, 33, 34).

The luminal narrowing imposed by valves increases the hydraulic resistance ($R_h$) that must be overcome to allow centripetal lymph progression along the lymphatic network. However, several studies suggest that intraluminal valves

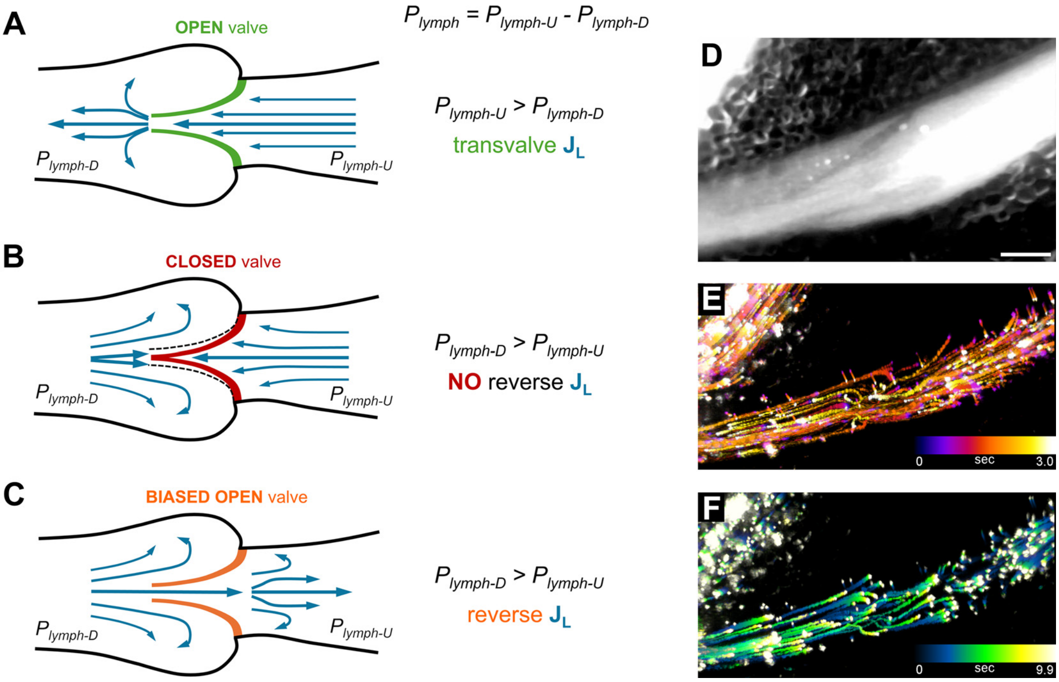

**Figure 1.** Schematic drawing of a valved lymphatic collecting segment showing the general view of the valve open-to-close cycle, displaying an intraluminal valve in an open (*A*, green), closed (*B*, red) or biased-open (*C*, orange) state. $P_{lymph\text{-}U}$, hydraulic pressure in the upstream segment; $P_{lymph\text{-}D}$, hydraulic pressure in the downstream segment; blue arrows indicate lymph flow ($J_L$). *D*: image of FITC-dextrans-filled diaphragmatic lymphatic collector, in which an intraluminal lymphatic valve is clearly identifiable. *E* and *F*: images of the MAX projection of microsphere position during an intrinsic flow cycle through the open-biased valve (*E*, forward progression; *F*, reverse flow) with the proper color timescale. Scalebar = 150 μm.

are biased toward the open position (Fig. 1*C*), probably to minimize resistance to lymph progression. This bias can lead to continuous valve openness within lymphangion chains, allowing some reverse flow and negatively affecting the overall efficiency of the lymphatic pump (Fig. 1, *D–F*) (6, 29, 33, 35). Moreover, when valves open and close asynchronously, this can have a beneficial effect on lymph propulsion, giving rise to higher pumping efficiency (36). The complex fluid dynamics in the valve region reveal high lymph velocity directed toward the valve axis, along with the formation of perivalvular recirculation zones characterized by low wall shear stress and large areas of flow stagnation. Furthermore, valves are a major source of nitric oxide (NO), whose shear stress-dependent release reduces spontaneous lymphatic contractility (6, 37, 38).

The present work aimed to further investigate the impact of lumen narrowing introduced by intraluminal valves of collecting vessels in the rat diaphragm. In this region, lymphatic valves are biased toward the open position during intrinsic spontaneous contractions, whereas they are forced into an open-to-close cycle by extrinsic forces, since skeletal muscle contractions impose larger changes in $\Delta P_{\mathrm{lymph}}$ (29). Comparative data on lymph flow, hydraulic pressure gradients, and hydraulic resistance derived from valved and nonvalved segments will provide deeper insights into the pivotal role of intraluminal valves in the physiology and pathophysiology of the lymphatic system.

## MATERIALS AND METHODS

### Surgical and In Vivo Procedures

All procedures were approved by the Animal Care and Use Ethics Committee of the University of Insubria (OPBA) and by the Italian Ministry of Health, in accordance with Italian D.Lgs 26/2014 (Experimental Protocol 698/2020). Wistar rats were raised in the in-house colony and housed in groups of two to three siblings in standard plastic cages equipped with transparent plastic shelters for environmental enrichment (Tecniplast SpA; Buguggiate, Varese, Italy). They had ad libitum access to food pellets and water and were maintained under a 12-h:12-h light-dark cycle.

Adult healthy Wistar rats of both sexes ($n = 10$; body weight = 393 ± 41 g) were deeply anesthetized with an intraperitoneal injection of a cocktail of sodium thiopental (50 mg/kg body wt, Pentothal Sodium, Intervet Productions Srl.) and medetomidine (0.5 mg/kg body wt, Medeson, TREI Spa) in saline solution. After an adequate depth of anesthesia was confirmed, in vivo fluorescent staining of the pleural diaphragmatic lymphatic network was performed using a well-established protocol (17, 29). A fluorescent mixture of 1% 250-kDa FITC-conjugated dextrans (fluorescein isothiocyanate, Ex/Em: 505/515; FD250S, Merck) and 1% tetramethylrhodamine isothiocyanate (TRITC)-fluorescent microspheres (TRITC; diameter: 1 µm; Ex/Em: 580/605; F8821, Invitrogen) in saline was intraperitoneally administered through a stainless-steel cannula (outer diameter ∼0.8 mm) inserted through the lateral abdominal wall and positioned in the subdiaphragmatic medial region.

Animals were placed prone on a heated blanket (37°C) and allowed to breathe spontaneously for 60 min after fluorescent dye injection, permitting diaphragmatic lymphatic vessels to drain the fluorescent mixture from the abdominal cavity so that the collectors would subsequently be visible under fluorescence in both FITC (for localization and clear detection of spontaneous contractility) and TRITC channels (for microsphere tracking).

They were then tracheotomized, and a T-shaped cannula was inserted into the trachea. Paralysis was induced with a 0.3-mL bolus of 2 mg/mL pancuronium bromide (P1918, Merck) in saline administered via the jugular vein, and animals were mechanically ventilated with room air at a tidal volume, and respiratory rate was automatically adjusted according to body weight (Inspira, Harvard Apparatus).

The chest wall was then opened, the pleural surface of the diaphragm was exposed, and fluorescent-stained lymphatics were visualized under a stereomicroscope (SV11, ×1 lens, Zeiss) equipped with a custom LED epi-illuminator (Luxeon Star high-intensity LEDs). Figure 2*A* shows a representative image of the lymphatic network of the diaphragm observed in epifluorescence. Tissue dehydration was prevented by periodic rinsing with gentle flushes of heated saline solution.

From each animal, 3 to 5 diaphragmatic tissue strips containing networks of lymphatic collectors (∼35–40 mm in length and 5–10 mm in width, longitudinally oriented with respect to the skeletal muscle fibers of the diaphragm to preserve tissue functionality) were excised from the costal margin to the central tendon and stored at 4°C in Petri dishes filled with cold HEPES-buffered Tyrode's solution (containing in mM: 119 NaCl, S7653; 5 KCl, P9541; 25 HEPES buffer, H3375; 2 $CaCl_2$, 21115; 2 $MgCl_2$, 63069; 33 D-glucose, G5767; pH 7.4; all from Merck; Cold Spring Harbor Protocols, https://doi.org/10.1101/pdb.rec10805) for subsequent ex vivo experiments. At the end of the surgical procedures, animals were euthanized with an overdose of the anesthetic cocktail.

### Ex Vivo Functional Recordings and Image Acquisition

Each diaphragmatic tissue sample was pinned to the bottom of a perfusion chamber (RC-27D, Warner Instruments), ensuring that the geometry and dimensions of the lymphatic network matched those observed in situ and preventing artifacts related to mechanical stresses that could influence lymphatic functionality (Fig. 2, *B* and *C*). The perfusion chamber was filled with oxygenated HEPES-buffered Tyrode's solution and placed on the stage of an upright fluorescence microscope (BX51WI, ×4 Plan APO objective, numerical aperture 0.13, Olympus). The temperature of the tissue in the perfusion chamber was continuously monitored using an implantable T-type thermocouple positioned as close as possible to the lymphatic network. It was maintained within ±0.1°C of the target value by the ITC100-VH PID thermostat (Inkbird), which controlled a resistive load incorporated into the recording chamber. The initial chamber temperature (∼20°C) was raised to a stable value of 37.0 ± 0.1°C. After a conditioning period of 3–5 min, video recordings of the lymphatic network were acquired for at least 3 min by alternately exciting FITC or TRITC fluorophores. This allowed the measurement of lymphatic vessel diameter (Fig. 2*D*) and microsphere progression along the vessels and in the valve region (Fig. 2, *E* and *F*), respectively. Diaphragmatic strips

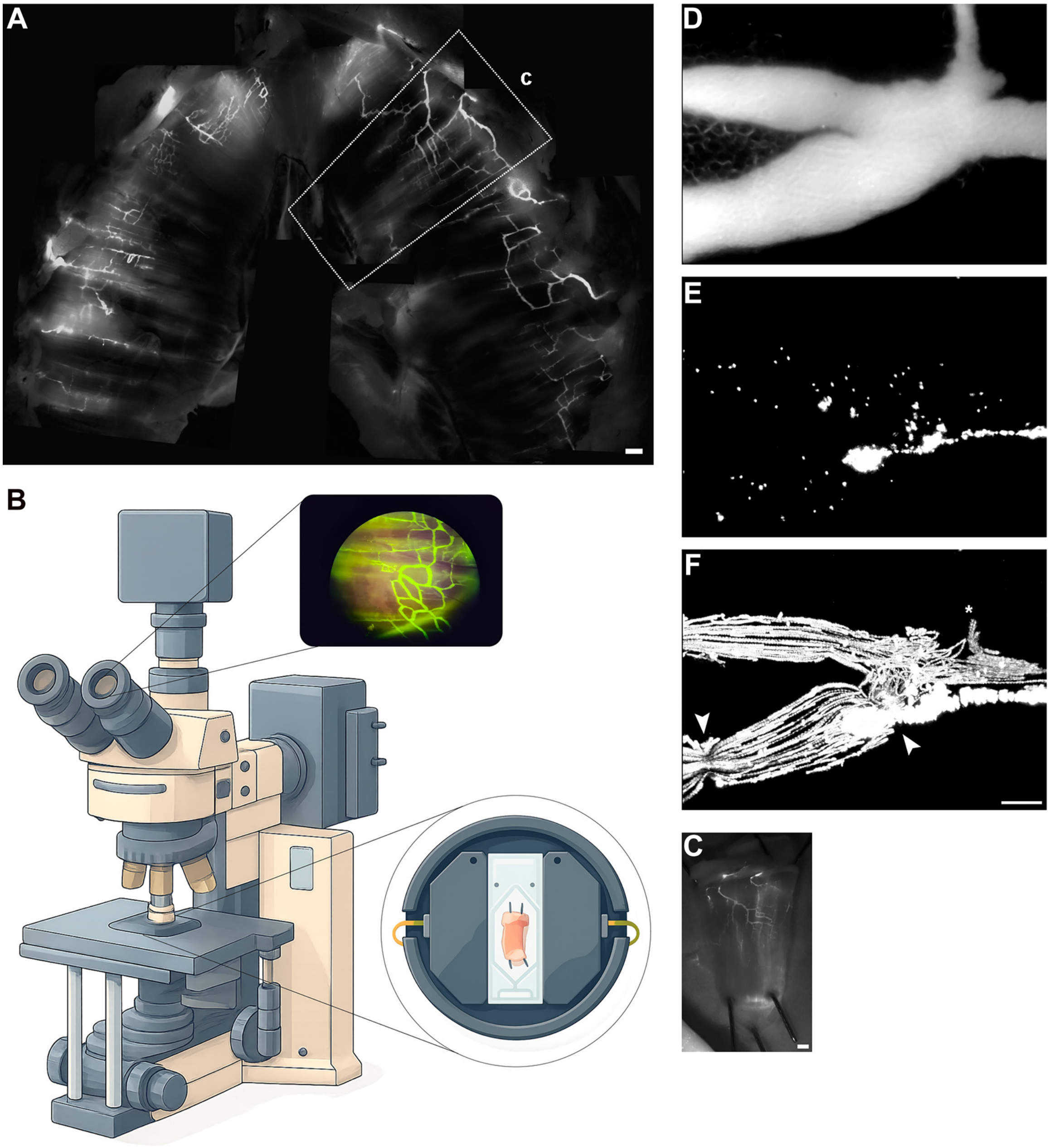

**Figure 2.** *A*: representative image of the fluorescent-stained lymphatic network over the rat diaphragm. The *inset c* highlights the tissue strip visualized in *C*. *B*: schematic drawing of the experimental setup. Fluorescent vessels in the tissue strip placed on the stage of the upright microscope can be identified on the dark background. *C*: diaphragmatic tissue strip pinned to the bottom of the perfusion chamber. *D*: representative image of a FITC-dextrans filled lymphatic collector, in which vessel edges are clearly identifiable and *d*D easily measurable. *E*: image of tetramethylrhodamine isothiocyanate (TRITC)-conjugated microspheres suspended in the vessel lumen. *F*: MAX projection of TRITC-conjugated microspheres progression along the same collecting vessel, in which single microspheres or aggregates can be optically resolved and tracked. The arrowheads indicate open valves, whereas the asterisk points to a closed valve. Scalebar (*A* and *C*) = 1 mm. Scalebar (*D*–*F*) = 150 μm.

containing no visible intrinsically contracting vessels at 37°C were discarded before recording began.

### Hydraulic Intraluminal Pressure ($P_{lymph}$) Measurements

Hydraulic intraluminal pressure ($P_{lymph}$, $cmH_2O$) was recorded ex vivo using the micropuncture technique (39). Tissue samples were obtained as previously described, except that fluorescent staining was performed with an intraperitoneal injection of 1% FITC-dextrans in saline alone to prevent microsphere aggregates from occluding the tip of the recording micropipette. Samples were then pinned to the bottom of an RC-27D perfusion chamber filled with HEPES-buffered Tyrode's solution and placed on the stage of a BX51WI microscope.

Borosilicate glass capillaries (1B100-4, outer diameter 1.0 mm, inner diameter 0.78 mm; WPI Europe) were pulled with a P-97 Flaming/Brown Micropipette Puller (Sutter Instrument) to obtain micropipettes, which were then beveled at 30° to a final tip diameter of ∼2.5 μm. Pipettes were backfilled with 2% Lissamine Green (L6382, Merck) dissolved in 1 M NaCl and secured to a pipette holder filled with 1 M NaCl. The holder was connected to a mineral oil-filled pressure transducer (Gould Instruments System), which was in turn connected to an electrohydraulic servonulling pressure measuring system (Servonull Pressure-Measuring System, Vista Electronics). $P_{lymph}$ traces were amplified (6600, Gould Electronics), digitized, and displayed on a monitor using custom-made LabVIEW software (National Instruments).

Each micropipette was calibrated in a modified Lucite box over the ±50 $cmH_2O$ range immediately before pressure recordings. The hydraulic pressure reference (0 $cmH_2O$) was set by immersing the pipette tip in the HEPES-Tyrode's solution filling the perfusion chamber, at the same level at which $P_{lymph}$ recordings were obtained. Intraluminal $P_{lymph}$ was recorded for at least 1 min by gently advancing the micropipette tip into the lymphatic vessel using a three-axis mechanical micromanipulator (M3301, WPI Europe). A pressure trace was considered suitable for analysis only if the zero reference pressure remained unaltered at the end of the procedure, otherwise, it was discarded.

Throughout the recordings, chamber temperature was maintained at 37.0 ± 0.1°C. Lymphatic vessels in which $P_{lymph}$ was measured were also video recorded for subsequent measurement of $d$D, as described in *Diameter and cross section of lymphatic vessels*. For each measurement, mean $P_{lymph}$ was calculated by integrating the pressure profile over time and dividing by the corresponding time interval. Intraluminal hydraulic pressure gradients ($\Delta P_{lymph}$) were computed as the difference in $P_{lymph}$ between two adjacent sites.

## Numerical Methods

### *Diameter and cross section of lymphatic vessels.*

Video recordings of FITC-filled lymphatic vessels ($n = 30$) were converted into black-and-white binary image sequences and analyzed offline using the automatic "diameter" plugin (40) of ImageJ Software (41), to obtain diameter ($d$D, μm) profiles over time. For contracting lymphatics, both end-diastolic ($d$D) and end-systolic ($d$S, μm) diameters were measured. The lymphatic cross sectional area ($S_L$, $\mu m^2$) was computed as follows:

$$S_L = \left[\left(\frac{dD}{2}\right) \times \left(\frac{dD}{2} \times 0.35\right)\right] \times \pi. \qquad (1)$$

In most fluid dynamics models, lymphatic vessels are simplified as circular cross sections for ease of calculation. However, pleural diaphragmatic lymphatics are elliptical (42). Based on functional measurements previously performed in situ, they display a transverse-to-parallel diameter ratio of 0.35 (39), where $d$D represents the vessel diameter lying in the plane parallel to the pleural diaphragmatic surface and ($d$D × 0.35) the perpendicular one. The panorama of the rat diaphragm, containing the fluorescent-filled lymphatic network was obtained by the semiautomated alignment of multiple adjacent images performed using the "MosaicJ" plugin of ImageJ Software (43).

### *Microspheres mean velocity and lymph flow.*

Video recordings of TRITC-conjugated microspheres moving along lymphatic vessels enabled visualization of lymph flow, and the Max Intensity Z-projection function (MAX) of ImageJ software was applied to the image sequences to identify intraluminal valves along the vessels. In FITC-filled vessels, valve leaflets are not always clearly visible nor is the point of maximum restriction evident (Fig. 1*D*). The MAX function allowed microsphere progression throughout the entire time interval to be displayed in a single image, highlighting any restrictions within the vessel lumen.

Video data were analyzed to measure the forward velocity of microspheres in a lymphatic tract upstream of intraluminal valves, corresponding to the site of $d$D measurement, during the entire forward phase. In each lymphatic tract ($n = 30$), the trajectories of five distinct, nonsimultaneous microspheres were manually tracked. The distance traveled (μm) was divided by the time interval required for each progression to obtain the mean forward velocity ($vel_{\text{-f}}$, μm/s).

To assess the laminarity of lymph flow, the unitless Reynolds number (Re) was computed as:

$$\mathrm{Re} = \frac{\delta \times vel_{\text{-f,MAX}} \times D_h}{\eta}, \qquad (2)$$

where $vel_{\text{-f,MAX}}$ is the maximal lymph velocity (m/s), $D_h$ is the hydraulic diameter (m), and δ and η are the lymph density (997 $kg/m^3$) and dynamic viscosity [0.0015 kg/(m·s)], respectively (44, 45). $D_h$ for an elliptical lymphatic vessel was calculated as 4 $S_L$/P, where P is the vessel perimeter computed using the first Ramanujan approximation.

For each vessel, forward-only lymph flow [$J_{L\text{-f}}$, nL/min] was computed as follows:

$$J_{L\text{-f}} = \frac{S_L \times vel_{\text{-f}}}{10^6}, \qquad (3)$$

where $10^6$ is the $\mu m^3$-to-nanoliter conversion factor. $J_{L\text{-f}}$ corresponds to the maximum lymph flow in a lymphatic tract, omitting possible reverse movement of microspheres suspended in lymph. However, oscillatory flow was clearly visible in most diaphragmatic lymphatic vessels and across intraluminal valves, which are biased toward the open position (29). $J_{L\text{-f}}$ data were plotted against their respective $d$D values to derive a relationship suitable for predicting lymph flow in any lymphatic vessel of known size.

Because of the unsteady nature of oscillatory lymph flow, the unitless Womersley parameter (α) was also computed as follows:

$$\alpha = r_h \times \sqrt{\frac{\delta \times \omega}{\eta}}, \qquad (4)$$

where $r_h$ is the hydraulic radius (m), calculated for an elliptical vessel as $S_L$/P, and ω the pulse angular frequency ($s^{-1}$), defined as $\omega = 2\pi f$, with $f = 0.32$ Hz, the mean spontaneous contraction frequency displayed by diaphragmatic collectors at 37°C (17).

Since the exact geometry of the narrowest valve section is elliptical (10, 46), its proportions are unknown. $D_h$ and $r_h$ were calculated across a range extending from a highly flattened elliptical section (transverse-to-parallel radius ratio $r{:}R = 0.01$) to a circular one ($r{:}R = 1$).

### *Microspheres instantaneous velocity and valve functional cross section.*

Based on images previously obtained using the MAX function, the progression of TRITC-conjugated microspheres along the prevalve lymphatic tract and across the adjacent intraluminal valve was manually tracked over a 1-s interval using the "Manual Tracking" plugin (https://imagej.net/ij/plugins/track/track.html) of ImageJ software. By tracking five nonsimultaneous microspheres in the prevalve region and five different microspheres crossing the valve during the same time intervals, frame-by-frame progression (µm) and velocity ($vel_{L\text{-}f}$ and $vel_{V\text{-}f}$, respectively, µm/s) were measured.

Since lymph flow is conserved when passing through adjacent lymphangions and across a valve, the product of velocity and vessel cross-sectional area remain constant. Therefore, the highest velocity of microspheres crossing the valve was used to estimate the valve functional cross section ($S_v$, µm$^2$), corresponding to the maximum narrowing offered to lymph passage.

For each vessel, $S_v$ was computed as:

$$S_V = \frac{S_L \times vel_{L\text{-}f}}{vel_{v\text{-}f}} \tag{5}$$

The maximum velocity of the microspheres in the prevalve and transvalve tracts was also used to compute the Reynolds number.

### *Hydraulic resistance ($R_h$) computation based on $P_{lymph}$ measurements.*

According to Poiseuille's law, fluid flow through a pipe (and thus lymph flow, $J_L$) is directly proportional to the pressure gradient that drives it ($\Delta P_{lymph}$, $cmH_2O$) and inversely proportional to the resistance that opposes it. Therefore, hydraulic resistance [$R_h$, ($cmH_2O \times s$)/nL] can be computed as the ratio of the measured pressure gradient to the lymph flow passing through the vessel or valve.

$$R_h = \frac{\Delta P_{lymph}}{J_L}. \tag{6}$$

$\Delta P_{lymph}$ data were plotted against the corresponding lymph flow ($J_L$), and $R_h$ was computed as the slope obtained from the data fit.

### Statistical Analysis

The present study includes two experimental groups of vessel segments: valved and nonvalved. All spontaneously contracting recorded vessels were included in the analysis, with no exclusions. Based on data from our previous work, we initially collected a minimum of 15 measurements per group and subsequently increased the sample size until a statistical power of ~0.9 was achieved.

All data are presented as mean ± standard error (SE). Statistics, power analysis, and data fitting were performed with SigmaPlot 10.0 software (Systat Software) and GraphPad PRISM 5. Statistical significance was assessed with the paired or unpaired Student's *t* test after data normality distribution check, and the threshold was set at $P < 0.05$.

## RESULTS

The analysis involved 30 diaphragmatic lymphatic collectors, in which intraluminal valves were identified. No large aggregates of microspheres were present that could have interfered with the subsequent analysis of lymph flow. Lymphatic vessels displayed a mean *d*D of 200.29 ± 14.06 µm and a mean vessel cross-sectional area ($S_L$) of 12,598 ± 1,692 µm$^2$. On average, each tissue strip contained 47 ± 3 lymphangions (range: 29–86; $n = 19$ strips) originating from 16 ± 1 lymphatic collectors. From each strip, we recorded a maximum of two to three vessels, selecting those that were spontaneously contracting, located sufficiently far from the strip edges such that several lymphangions in series separated the pressure measurement sites from the open ends and superficial enough to allow clear visualization of individual microsphere movements.

Figure 2*D* shows a bifurcating lymphatic vessel observed under FITC epifluorescence, which clearly defines the vessel edges. In Fig. 2*E*, the same lymphatic vessel was observed under TRITC epifluorescence and recorded over multiple intrinsic contraction cycles. Microspheres suspended in the vessel lumen (i.e., lymph) were transported along the vessel by intrinsically driven lymph flow. The trails visible in Fig. 2*F* result from a maximum gray value projection (MAX) across the entire recording. At valve sites, microsphere trails converged to pass through the valve (arrowheads, open valve) or displayed rounded trajectories when the valve was closed (asterisk). As reported numerically later in the text, and even by visual inspection, microsphere trails were parallel, indicating laminar flow even at valve sites.

### Functional Section of the Intraluminal Valve

Using *Eq. 5* to compute the valve functional cross section ($S_v$) required a series of preliminary measures regarding microsphere displacement. Figure 3 shows an example of five different microsphere progressions tracked over 2 s, during their movement in a vessel segment devoid of any intraluminal valve (Fig. 3*A*) and during passage through an adjacent valve (Fig. 3*B*). The steepest portion of the traces in Fig. 3*B* indicates passage through the narrowest cross section of the valve. From these data, a frame-by-frame calculation of microsphere velocity was performed (Fig. 3*C* for a nonvalved tract and Fig. 3*D* for a valved segment).

Overall, the mean velocity of microspheres in the nonvalved vessel segment ($vel_{L\text{-}f}$) was 209.54 ± 14.86 µm/s, whereas their velocity during transit through the narrowest area of the adjacent valve ($vel_{V\text{-}f}$) was 1617.29 ± 157.89 µm/s, a statistically significant increase (Fig. 3*E*, $P < 0.01$, paired *t* test, $n = 30$ vessels, Cohen's $d = 1.62$, power = 0.99).

Since volumetric flow is given by the product of cross-sectional area and velocity (*Eq. 3*) and because flow is conserved between two adjacent lymphangions divided by an intraluminal valve, the valve functional cross section ($S_v$) can be derived from the cross-sectional area of the nonvalved segment ($S_L$, obtained from *Eq. 1*) scaled by the velocity ratio (see MATERIALS AND METHODS, *Eq. 5*).

Figure 4*A* shows mean $S_L$ and $S_v$ (1,607 ± 192 µm$^2$ vs. 12,598 ± 1,692 µm$^2$ for $S_L$, $P < 0.01$, paired *t* test, $n = 30$, Cohen's $d = 1.178$, power = 0.99). Interestingly, when $S_v$ was plotted against the $S_L$ of its adjacent vessel tract, a linear correlation between them became evident (Fig. 4*B*). Data points in the *d*D range of 86–322 µm could be fitted by the following linear regression:

$$S_V = 0.103 \times S_L + 309.6 \tag{7}$$

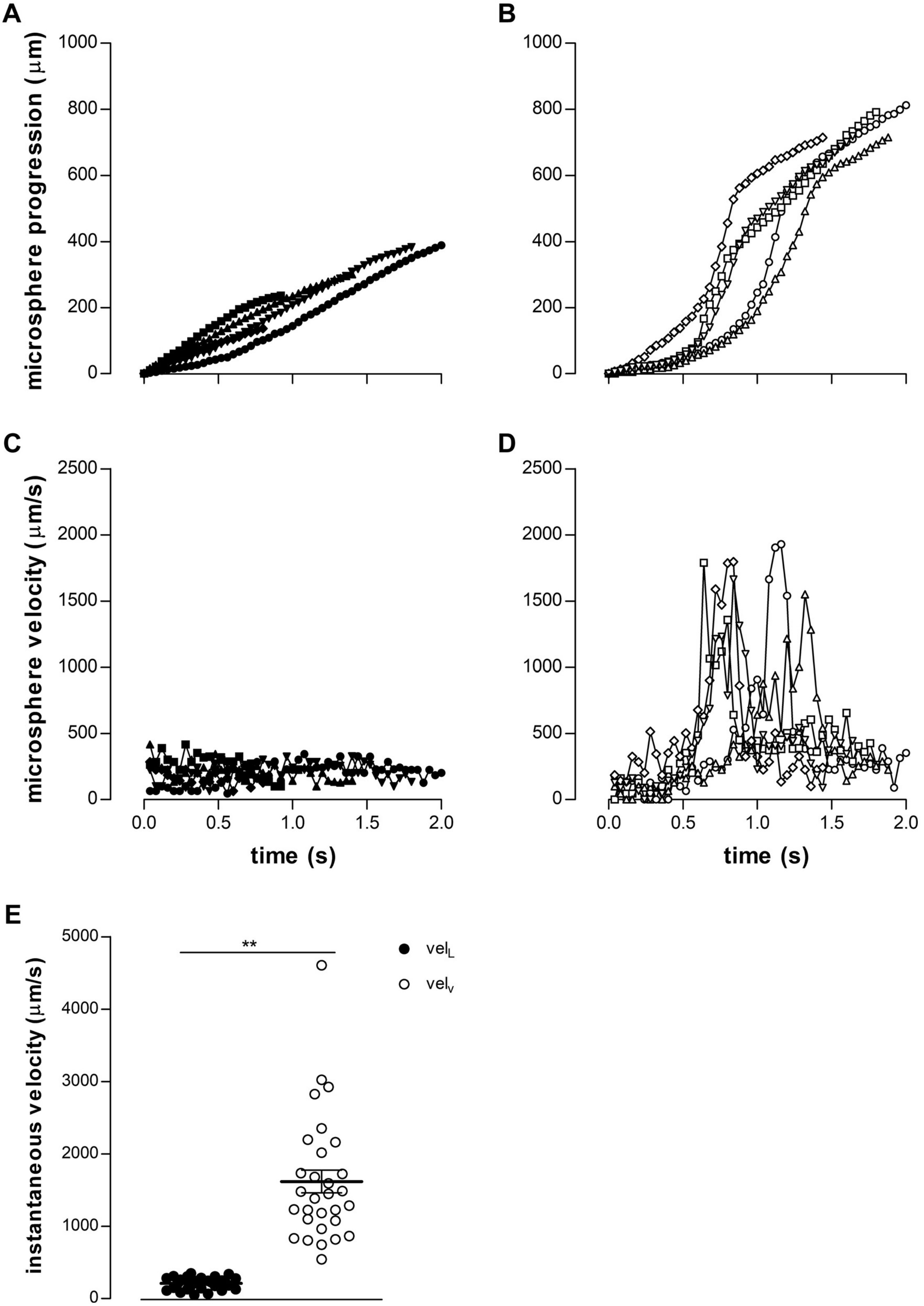

**Figure 3.** Microspheres tracked in a lymphatic tract devoid of intraluminal valves (*A* and *C*) or crossing the valve (*B* and *D*) to obtain their progression and velocity. *A*: representative traces of 5 microspheres progression in the nonvalved segment. The slope of the traces remains constant. *B*: representative traces of 5 different microspheres progressing across the lymphatic valve. The slope of the traces increases as the microspheres enter the intraluminal valve. *C*: representative traces of vel$_{L\text{-}f}$ of the 5 microspheres tracked in *A*. The mean velocity is constant and similar for all the microspheres tracked. *D*: representative traces of vel$_{v\text{-}f}$ of the 5 microspheres crossing the valve tracked in *B*. The microspheres' velocity dramatically increases as the microspheres enter the lymphatic valve. The velocity peaks correspond to crossing the narrowest area of the valve. *E*: microspheres' velocity tracked in the nonvalved lymphatic collector (solid dots) and crossing the adjacent intraluminal valve (hollow dots). $^{**}P < 0.01$ paired *t* test, $n = 30$ vessels.

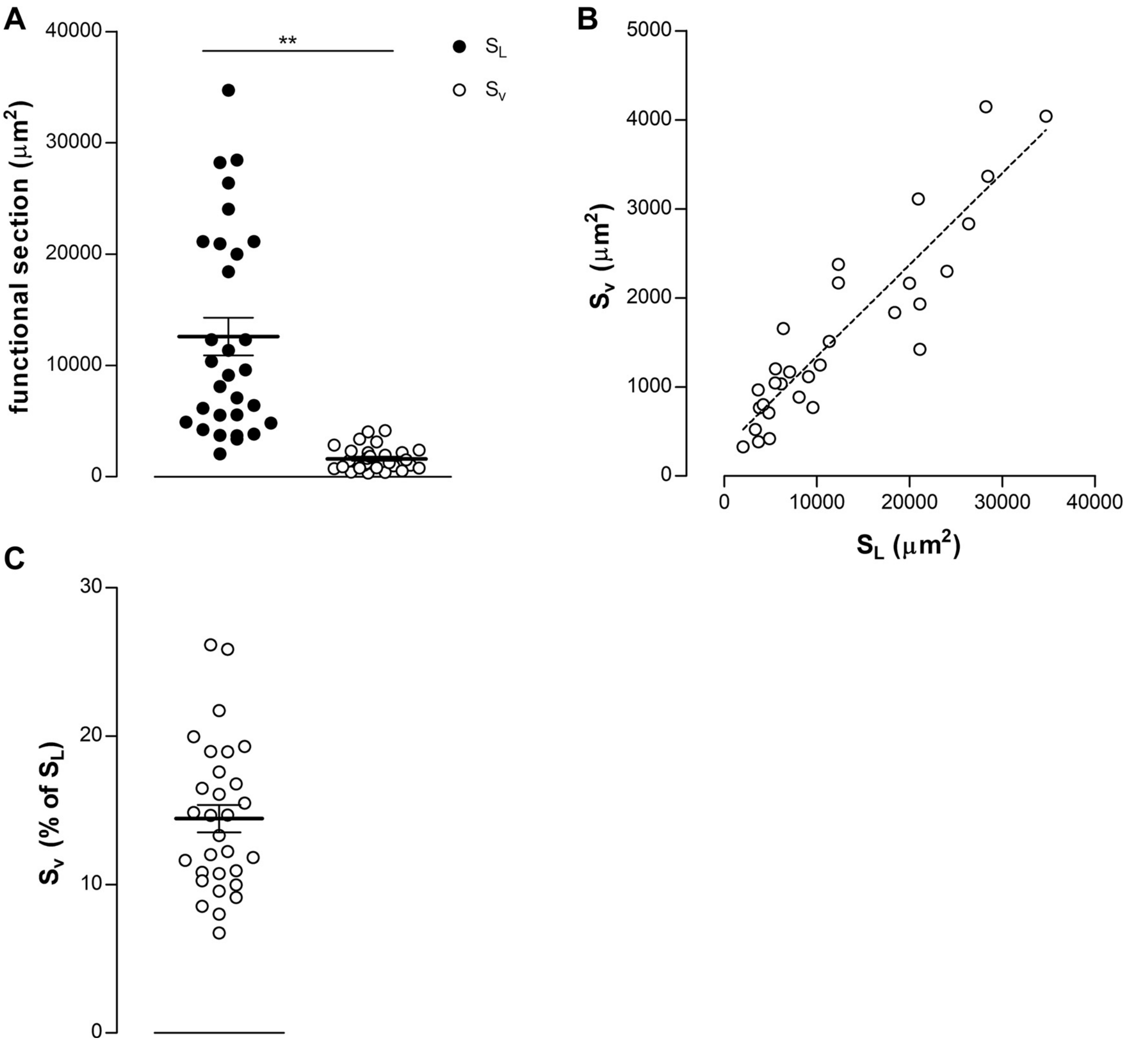

**Figure 4.** *A*: estimated functional section of lymphatic collectors ($S_L$, filled dots) and intraluminal valves ($S_v$, hollow dots). *B*: linear correlation between the valve functional section $S_v$ and the corresponding $S_L$, $r^2 = 0.82$. *C*: $S_v/S_L$ ratio expressed as percentage of $S_L$, which stands at around 14% of $S_L$. $^{**}P < 0.01$ paired *t* test, $n = 30$ vessels.

with $r^2 = 0.82$. This relationship held true for the entire range of vessel *d*D measured in the present study and, more generally, for lymphatics lying on the pleural surface of the diaphragm. On average, $S_v$ was 14.4 ± 0.9% of $S_L$ (Fig. 4*C*, $n = 30$ vessels).

## Relationship between Diastolic Diameter and Forward Lymph Flow

Simultaneous measurement of microsphere velocity (to derive lymph flow from vessel cross-sectional area) and intraluminal hydraulic pressure difference at two sites along the vessel proved unreliable due to technical artifacts. Microspheres suspended in the lymph lumen frequently occluded the tip of the glass micropipette used for $P_{lymph}$ measurement, whereas the pipette tip protruding into the vessel forced microspheres to alter their trajectory, artifactually affecting their velocity profile.

To overcome these limitations, a mathematical relationship between vessel diastolic diameter (*d*D) and forward lymph flow ($J_{L\text{-}f}$) was derived, allowing intraluminal $P_{lymph}$ to be recorded without using microspheres. In Fig. 5, $J_{L\text{-}f}$ values calculated from *Eq. 3* in nonvalved tracts were plotted against vessel *d*D. The dotted line represents the best parabolic fit of $J_{L\text{-}f}$ as a function of *d*D:

$$J_{L\text{-}f} = 0.001672 \times dD^2, \tag{8}$$

with an $r^2 = 0.79$ ($n = 30$ vessels).

This approach made it possible to reliably measure intraluminal hydraulic pressure and compute $J_{L\text{-}f}$ for subsequent analyses, starting from the measured *d*D of the vessel under investigation.

## Pressure Gradients in Open-Vessel Segments and across Intraluminal Valves

Using the micropuncture technique, intraluminal $P_{lymph}$ (Fig. 6*A*) and the pressure gradient ($\Delta P_{lymph}$, Fig. 6*B*) between two adjacent sites ~500 µm apart were measured in 20 nonvalved vessel tracts (*d*D = 176.56 ± 9.53 µm) and across 16 valved segments (*d*D = 157.15 ± 12.92 µm, not significantly different from *d*D of nonvalved tracts, $P = 0.225$, unpaired *t* test, $n = 36$), maintaining the same intersite

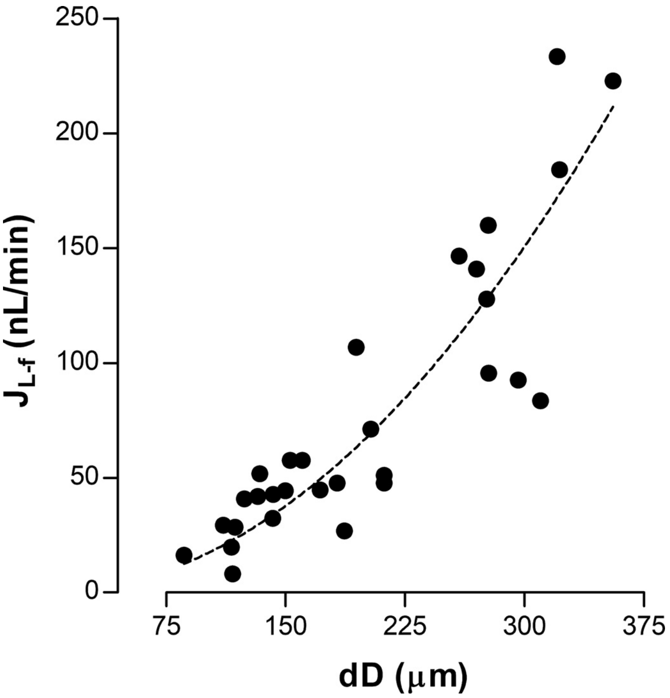

**Figure 5.** Parabolical distribution of forward lymph flow ($J_{L\text{-}f}$) plotted as a function of diastolic diameter *d*D. $r^2 = 0.79$, $n = 30$ vessels.

distance. As shown in Fig. 6*B*, $\Delta P_{\mathrm{lymph}}$ was significantly higher across valved segments than in nonvalved tracts (4.15 ± 0.57 cmH$_2$O vs. 2.16 ± 0.27 cmH$_2$O, $P < 0.01$, unpaired *t* test, $n = 36$, Cohen's $d = 0.744$, power $= 0.87$). Intraluminal $P_{\mathrm{lymph}}$ oscillations due to intrinsic lymphatic contractions averaged 1.93 ± 0.35 cmH$_2$O (Fig. 6*A*). Although $\Delta P_{\mathrm{lymph}}$ values showed some scatter, the minimum in nonvalved segments (0.43 cmH$_2$O) was lower than the minimum across valves (1.07 cmH$_2$O). The same applied to maximal values (4.33 cmH$_2$O vs. 7.49 cmH$_2$O). On average, the presence of a valve added 1.99 ± 0.93 cmH$_2$O to $\Delta P_{\mathrm{lymph}}$ to sustain the same lymph flow as a nonvalved segment of equal length.

### Forward and Reverse Flow Direction in Nonvalved and Valved Vessel Segments

Direct pressure measurements showed that intraluminal valves increase the pressure gradient required to overcome their added resistance to lymph flow. However, because valves remain biased toward the open position (at least under intrinsically driven flow), reverse flow is also observed, as previously reported by our group and others (29, 33, 34). To evaluate this phenomenon, progression, velocity, and flow were compared between nonvalved and valved segments.

For each valved vessel ($n = 30$), at least three microspheres passing through the valve were manually traced during three complete contraction cycles, following both forward and reverse trajectories. The same analysis was performed on 15 nonvalved segments (mean $dD = 201.20$ ± 17.16 μm, $P = 0.9691$ vs. valved vessels, unpaired *t* test, $n = 45$). From forward and reverse distances, respective velocities and the net velocity were derived. Because the average cross-sectional area remained the same during forward and reverse motion, net $J_L$ relative to forward flow ($J_{L\text{-}f}$) could be calculated from *Eq. 3*.

As shown in Fig. 7*A*, net progression relative to forward progression differed significantly between conditions, averaging 13.0 ± 2.2% in nonvalved segments and 53.2 ± 7.2% across valves ($P < 0.01$, $n = 45$ tracts, Cohen's $d = 1.23$, power $= 0.96$). When plotted against *d*D, the advantage of valves became evident. In valved segments (Fig. 7*B*, hollow dots), relative net progression increased linearly with *d*D:

$$\mathrm{net}_{+\,\mathrm{valve},\%} = 0.165 \times dD + 20.2, \tag{9}$$

with an $r^2 = 0.99$. In contrast, in nonvalved segments (Fig. 7*B*, filled dots), relative net progression decreased with *d*D:

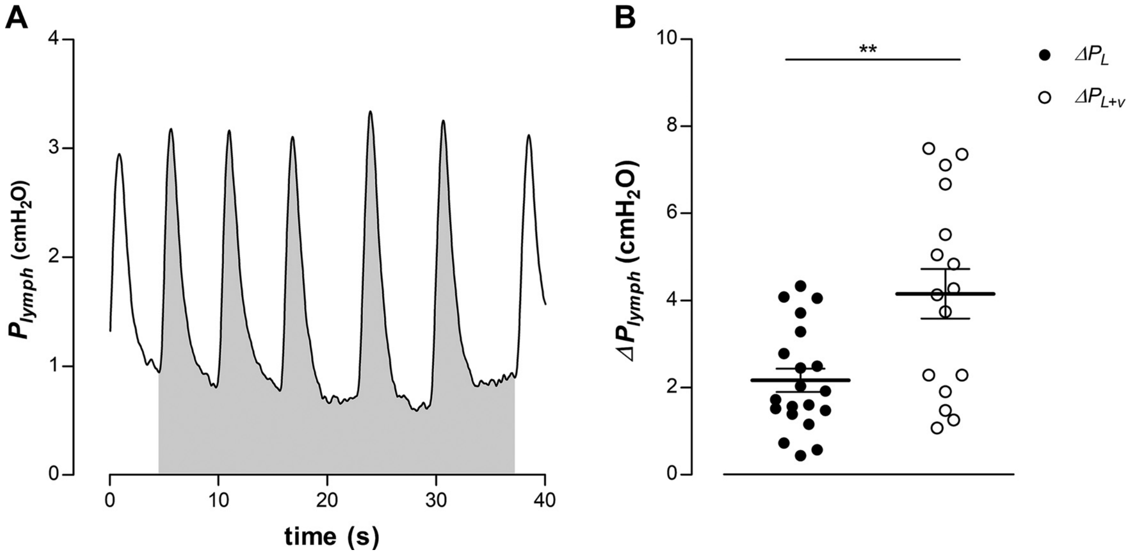

**Figure 6.** *A*: representative tracing of lymphatic intraluminal pressure ($P_{\mathrm{lymph}}$) in a vessel tract displaying $P_{\mathrm{lymph}}$ swings. Mean $P_{\mathrm{lymph}}$ was obtained by integrating the pressure trace (gray area) divided by the corresponding time interval. *B*: pressure gradients ($\Delta P_{\mathrm{lymph}}$) measured in lymphatic tracts devoid of valves ($\Delta P_L$ filled dots, $n = 20$ vessels) and in valved vessels ($\Delta P_{L+v}$ hollow dots, $n = 16$ vessels). $\Delta P_{\mathrm{lymph}}$ is the $P_{\mathrm{lymph}}$ difference measured between 2 adjacent sites ~500 μm apart. $^{**}P < 0.01$ unpaired *t* test.

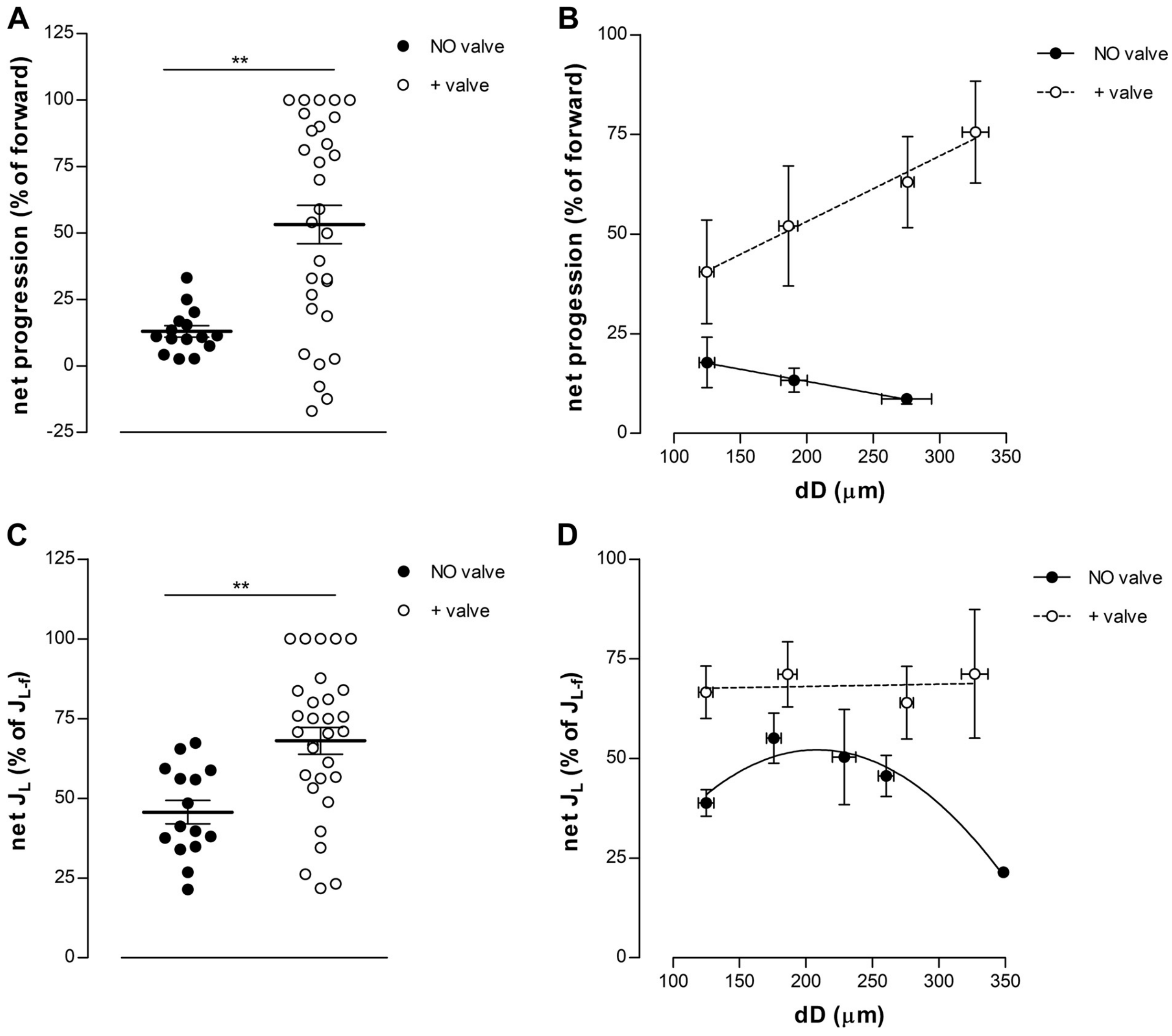

**Figure 7.** *A*: net microspheres' progression during a contraction cycle, expressed as a percentage of forward progression in nonvalved segments (filled dots) and crossing an intraluminal valve (hollow dots). *B*: dependence of net progression, expressed as percentage of forward progression, on *d*D, in nonvalved vessels (filled dots and solid line) and in lymphatics equipped with an intraluminal valve (hollow dots and dashed line). *C*: net lymph flow $J_L$ due to spontaneous contractions, expressed as a percentage of forward flow $J_{L\text{-}f}$ in nonvalved segments (filled dots) and crossing an intraluminal valve (hollow dots). *D*: parabolical downward distribution of net lymph flow $J_L$ plotted as a function of diastolic diameter *d*D in nonvalved segments (filled dots and solid line, $r^2 = 0.95$) and linear fit of flat net $J_L$ distribution in lymphatic tract displaying intraluminal valves (hollow dots and dashed line, $r^2 = 0.02$). Nonvalved segments, $n = 15$; valved vessels, $n = 30$; $^{**}P < 0.01$ unpaired *t* test.

$$\text{net}_{\text{NO valve},\%} = -0.061 \times d\text{D} + 25.2, \tag{10}$$

with an $r^2 = 0.98$, suggesting that larger nonvalved vessels are less efficient at lymph progression.

Consequently, two distinct net $J_L$ values emerged (Fig. 7*C*): 45.7 ± 3.7% of $J_{L\text{-f}}$ in nonvalved segments versus 68.0 ± 4.2% when a valve was present. Both net progression and net flow were significantly higher in valved than in nonvalved tracts ($P < 0.01$, unpaired *t* test, $n = 45$, Cohen's $d = 1.09$, power $= 0.92$). Interestingly, when relative net $J_L$ (% of $J_{L\text{-f}}$) was plotted against vessel *d*D, different trends were observed. In valved segments (Fig. 7*D*, hollow dots), net $J_L$ appeared independent of *d*D, with a regression slope not significantly different from zero:

$$J_{L,+\text{valve},\%} = 0.0057 \times d\text{D} + 66.91, \tag{11}$$

with an $r^2 = 0.02$.

In nonvalved tracts (Fig. 7*D*, filled dots), data were best fitted by a downward parabola:

$$J_{L,\text{NO valve},\%} = -0.0016 \times d\text{D}^2 + 0.67 \times d\text{D} - 17.71, \tag{12}$$

with an $r^2 = 0.95$, indicating vessel size dependence of net $J_L$.

The parabola peak (i.e., maximal relative net $J_L$) occurred at $d\text{D} = 209$ μm, within the most common range of diaphragmatic lymphatic diameters [45.56–375.91 μm, $n = 202$ vessels, data from previous works (15, 17–19, 47)]. Notably, some negative net progressions were observed in valved segments (Fig. 7*A*, hollow dots). However, because reverse velocities were always lower than forward ones (Fig. 8), net $J_L$ remained positive in all cases. Overall, the presence of a valve increased net $J_L$ by 22% compared with nonvalved segments.

Finally, the effect of intraluminal valves was assessed in the subset of vessels where $P_{\text{lymph}}$ was also measured. Although valves increased resistance, as confirmed by the

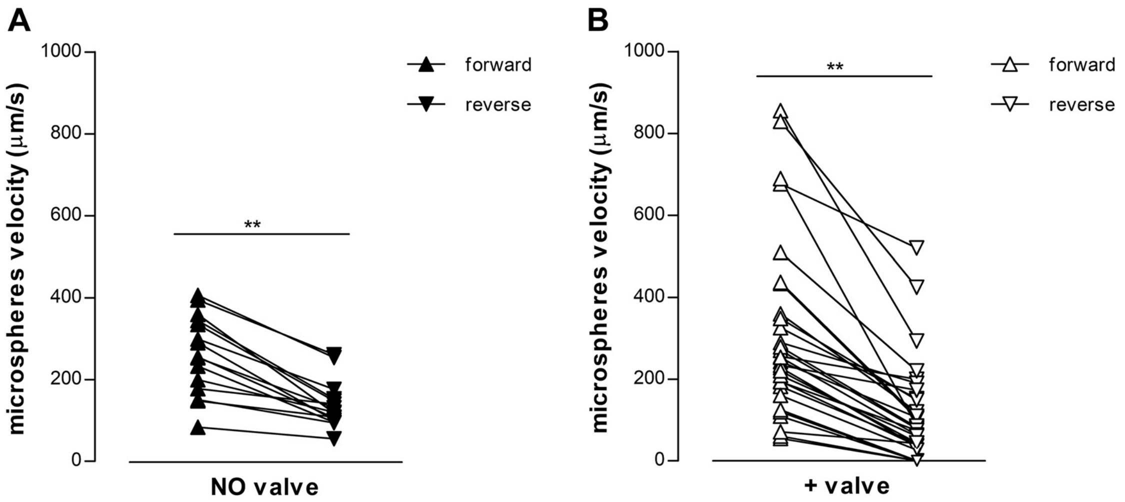

**Figure 8.** Mean forward (upward triangles) and reverse (downward triangles) velocity in lymphatic vessels devoid of valves (*A*, filled triangles, $n = 15$) or equipped with an intraluminal valve (*B*, hollow triangles, $n = 30$). In all tested vessels, the forward velocity was always higher than the reverse velocity. $^{**}P < 0.01$ reverse vs. forward, paired *t* test.

higher $\Delta P_{lymph}$ required to sustain flow, results in Fig. 7*C* demonstrate their positive contribution to net lymph transport. To further evaluate this effect, absolute net $J_L$ was modeled for lymphatics spanning the typical *d*D range of the rat diaphragmatic network (75–375 μm). Forward $J_{L\text{-}f}$ was calculated from *Eq. 8* for each vessel segment as a function of *d*D, and net $J_L$ was then derived using *Eq. 9* or *Eq. 10* for valved and nonvalved tracts, respectively. Results are shown in Fig. 9*A* in valved lymphatics, where $\Delta P_{lymph}$ was directly measured ($n = 16$), $J_L$ was consistently higher than in nonvalved tracts ($n = 20$), regardless of *d*D. However, across the entire population of vessels examined, mean $J_L$ did not differ significantly between nonvalved and valved segments (26.9 ± 3.2 vs. 30.9 ± 5.4 nL/min, respectively, $P = 0.5084$, unpaired *t* test, $n = 36$; Fig. 9*B*). This outcome was expected, as valved and nonvalved segments are interspersed throughout the diaphragmatic lymphatic network.

## Reynolds Number and Womersley Parameter

The Reynolds number (Re; Fig. 10*A*) was computed in both the prevalve segment and the narrowest valve tract. In the nonvalved segment, Re was 0.026 ± 0.003, whereas in the valved tract, it was higher but never exceeded 0.048 ± 0.006 ($n = 30$). Because Re $\ll 1$ under all conditions, laminar lymph flow in diaphragmatic lymphatics was confirmed even at maximum valve narrowing. This finding suggests that intraluminal valves do not introduce significant turbulence into overall flow dynamics.

The Womersley parameter (α; Fig. 10*B*) was also computed in both the prevalve segment and the narrowest valve tract. In the nonvalved segment, α was 0.029 ± 0.002, whereas in the valved tract, it was lower and never exceeded 0.012 ± 0.001 ($n = 30$). These very low α values indicate that lymph flow in diaphragmatic collectors is mainly governed by low-frequency oscillations, viscous forces, and pressure drop.

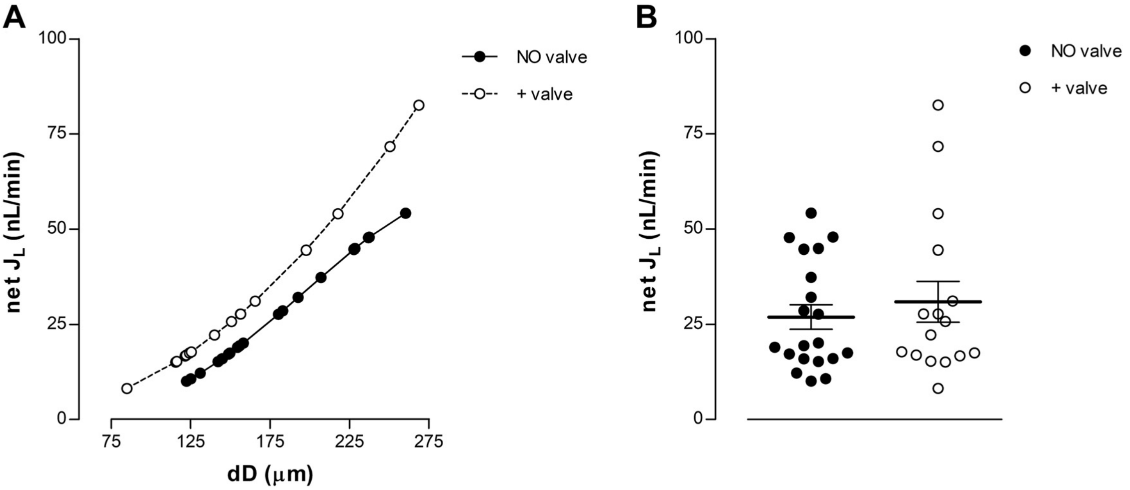

**Figure 9.** *A*: computed net lymph flow (net $J_L$) in nonvalved lymphatic segments (filled dots and solid line, $n = 16$) and in vessels displaying an intraluminal valve (hollow dots and dashed line, $n = 20$), obtained by combining *Eq. 8* with *Eq. 10* or *Eq. 9*, respectively. *B*: mean computed net lymph flow in the 2 different populations of collecting vessels.

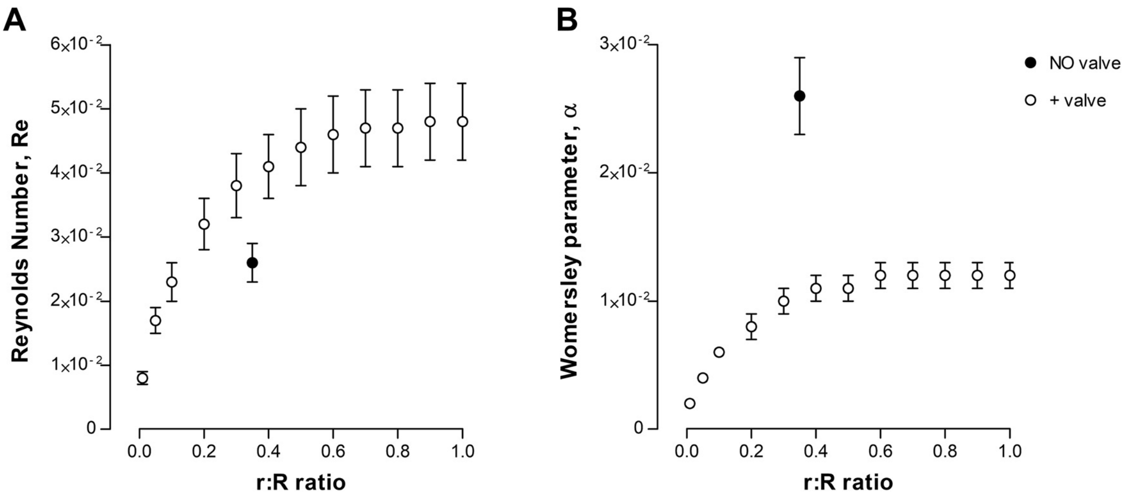

**Figure 10.** Computed Reynolds number (*A*) and Womersley parameter (*B*) in ellipse-shaped nonvalved diaphragmatic lymphatic vessels, having a fixed *r:R* ratio of 0.35 (filled dots, $n = 30$) and in the narrowest valve area, computed in the *r:R* ratio range 0.01–1 (hollow dots, $n = 30$).

### Hydraulic Resistance

From a functional standpoint, net flow ($J_L$) is the relevant parameter to quantify lymph progression from diaphragmatic tissue and the pleural cavity. According to the Hagen–Poiseuille law, $R_h$ can be estimated from *Eq. 6* for each valved and nonvalved vessel segment. $\Delta P_{lymph}$ and $J_L$ data for nonvalved ($n = 20$) and valved ($n = 16$) segments were plotted (Fig. 11), and $R_h$ was computed as the slope obtained from data fitting.

For nonvalved lymphatics (Fig. 11*A*), the linear fit yielded an $R_h$ of $-0.256$ cmH$_2$O·s/nL, whereas for valved segments (Fig. 11*B*), $R_h$ was $-3.944$ cmH$_2$O·s/nL.

This result demonstrates that valves play a pivotal role in enabling unidirectional net lymph transport in collecting lymphatics. At the same time, their hindrance to flow decreases with increasing lymph flow, a key feature that optimizes transport under the low-pressure, low-flow conditions sustained by intrinsic contractility alone.

## DISCUSSION

The present study quantified the effect of intraluminal lymphatic valves in the diaphragmatic network on lymph flow driven exclusively by the intrinsic mechanism. In a highly branched lymphatic network, where the extrinsic mechanism predominates due to the continuous motion of the diaphragmatic dome, heart, and chest wall (29), it has remained unclear whether valves hinder or facilitate intrinsically driven lymph progression, which occurs primarily in the lymphatic vessels of the muscular periphery of the diaphragm.

### Lymph Flow Velocity by Particle Tracking

In the ex vivo experimental preparation, lymphatic valves were faintly visible as dovetail-shaped structures in FITC-stained vessels (Fig. 1*D*). To confirm their presence and role, TRITC-labeled microspheres resuspended in lymph were used to track intravascular trajectories, supported by intrinsic motion occurring elsewhere along the vessel (Fig. 1, *E–F* and Fig. 2*F*). Measurements of the instantaneous forward motion of microspheres driven by lymph revealed steady progression in nonvalved vessel tracts, whereas in valved segments, progression showed a sudden change in slope—and therefore flow velocity—during transit through the open section of the intraluminal valve (Fig. 3, *A* and *B*). Microsphere forward velocity averaged ~209 μm/s in nonvalved tracts and ~1,617 μm/s when crossing the valve (Fig. 3*E*). Both values fall within the lower range of velocities reported in rat mesenteric lymphatics as shown by Dixon et al. (45) or obtained in computational models (48, 49). However, mesenteric lymphatics and computational models involve vessels with circular rather than elliptical cross sections, unlike diaphragmatic vessels (39, 42). The equivalent diameter of a vessel with the cross-sectional area of the analyzed diaphragmatic lymphatic was 118 μm, which may represent a more appropriate basis for comparison with data from nonelliptical vessels.

Despite the lower velocity observed in diaphragmatic lymphatics, several factors may contribute to this phenomenon. First, the intricate branching pattern surrounding the investigated vessel segments may influence lymph flow dynamics. Second, the elliptical shape of the vessels confers distinctive hydraulic properties, potentially affecting lymph transport. Third, the diaphragmatic lymphatic network exhibits unique characteristics, in which intrinsic contractions are not the primary mechanism of lymph transport. These observations provide additional evidence of the variability and versatility of the lymphatic network as a whole. Microspheres (and thus lymph) are subjected to acceleration as they transit through the open valve orifice, an observation already reported by others (50). The difference between flow velocities before and during valve transit was later used to describe transvalve flow dynamics in greater detail.

### Intraluminal Valve Functional Section

Several detailed and elegant reports have provided three-dimensional (3-D) reconstructions and models of intraluminal lymphatic valves in open states, showing the slit-like orifice and the biased-open configuration when the hydraulic pressure gradient across the valve was zero or near zero (10,

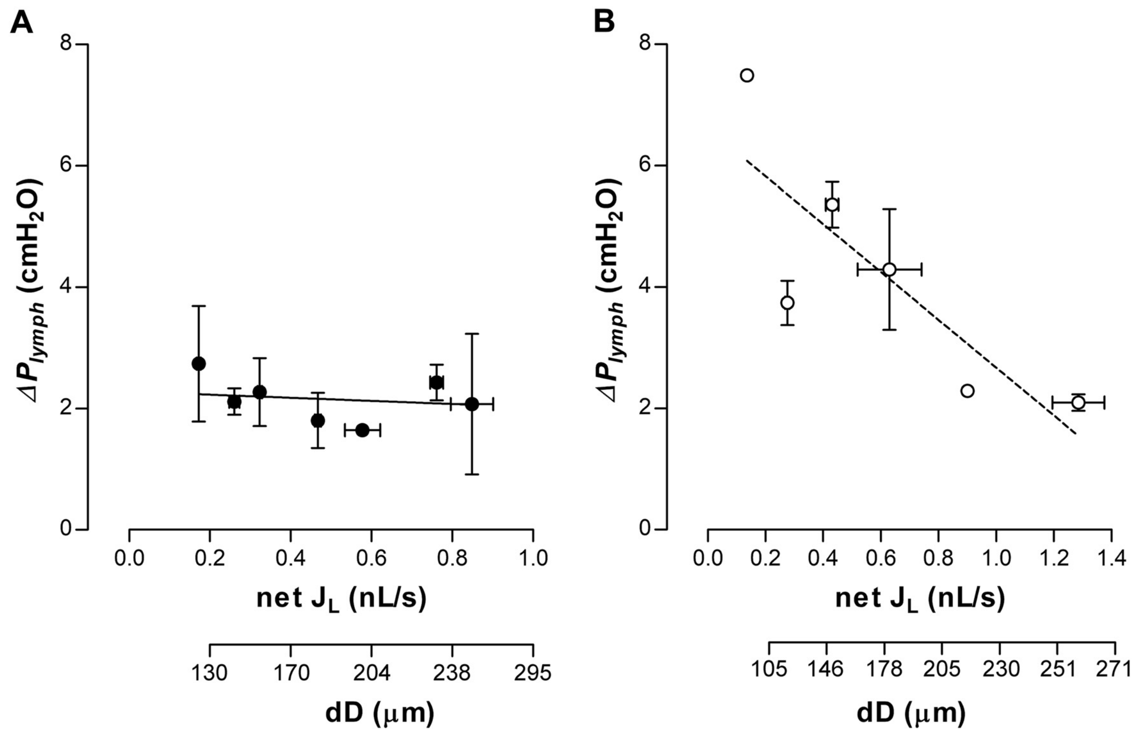

**Figure 11.** Plot of pressure gradient data ($\Delta P_{lymph}$) vs. corresponding net lymph flow (net $J_L$) and vessel size (*d*D, secondary *x*-axis) in nonvalved lymphatic vessels (*A*, filled dots, $n = 20$) and in vessels equipped with an intraluminal valve (*B*, hollow dots, $n = 16$). The slope of the linear fits ($\Delta P_{lymph}$/net $J_L$) represents the hydraulic resistance ($R_h$) for nonvalved (solid line, $r^2 = 0.01$) and valved segments (dashed line, $r^2 = 0.69$).

33, 51). From this body of literature, it is clear that the exact shape of the valve orifice cannot be unambiguously determined, whereas the functional effects of valve opening, closing, or a prolonged biased-open state are evident from the motion of lymph (i.e., the suspended particles) through the valve.

The velocity of microspheres within the valve compared with the nonvalved segment provided a useful tool to assess the corresponding change in cross-sectional area. Since fluid flow can be calculated as the product of flow velocity and cross-sectional area, and lymph flow is conserved between two adjacent vessel tracts—one of which contains an intraluminal valve—the functional section of the valve ($S_v$) was quantified using the velocity ratio (Fig. 4*A*). The ratio of $S_v$ to the vessel cross-sectional area $S_L$ in the investigated diaphragmatic vessels averaged 0.14 (Fig. 4*C*), closely matching the 1:7 ratio reported by Davis et al. (33) in mesenteric lymphatics. A vessel-by-vessel analysis also revealed a linear relationship between $S_v$ and $S_L$ with a slope of ~0.1 (Fig. 4*B*). This finding represents a novel contribution to the literature, since previous studies assessed valve opening in relation to vessel distention or lymph flow, but not in a population of physiologically distended vessels of different sizes (33, 51–53).

### Relationship between Lymph Flow and Vessel Diameter

Viscous resistance is an important parameter in fluid dynamics. According to Poiseuille's law for laminar flow, it can be obtained as the ratio between the pressure gradient and the resulting fluid flow. The actual hindrance to intrinsically driven lymph flow was therefore estimated by attempting simultaneous recordings of particle motion and intraluminal pressure gradients in nonvalved vessel tracts and across intraluminal valves. However, reliable $P_{lymph}$ recordings in vessels containing fluorescent microspheres could not be obtained due to technical artifacts, as microspheres randomly occluded the pipette tip used for pressure measurements or were diverted by the pipette itself, thereby altering their trajectory and artifactually affecting velocity measurements. An alternative approach was therefore pursued to obtain lymph flow and correlate it with intraluminal $\Delta P_{lymph}$, avoiding the simultaneous use of both techniques.

Forward lymph flow (derived from the combined use of *Eqs. 1* and *3*) was plotted as a function of the corresponding vessel diameter. As shown in Fig. 5, data were best fitted by a parabolic relationship with a coefficient of ~0.0017 nL/(min·µm$^2$), reflecting the elliptical geometry of lymphatics in the experimental model, their extensive branching, and the lower prevalence of intrinsic pumping in diaphragmatic vessels.

### Intraluminal Pressure Gradients ($\Delta P_{lymph}$) in Nonvalved Segments and across Intraluminal Valves

Intraluminal $P_{lymph}$ measurements obtained between two sites ~500 µm apart, either along nonvalved segments or across intraluminal valves, displayed classical oscillatory behavior due to intrinsic contractions upstream of the measurement site. From $P_{lymph}$ traces such as that shown in Fig. 6*A*, mean local $P_{lymph}$ values were calculated as the ratio between the time integral of at least five consecutive contraction cycles and the elapsed time. $P_{lymph}$ swings due to intrinsic contractions were ~2 cmH$_2$O, a very low value considering that extrinsic contractions of the diaphragmatic skeletal muscle can induce variations in intraluminal pressure of ~10–20 $cmH_2O$ (54). Since lymph backflow does not occur in the presence of extrinsic contractions (29), this change in $P_{lymph}$ appears to be necessary and sufficient to switch valve behavior from the biased-open state to an open-to-closed cycle. $\Delta P_{lymph}$ values were then computed for nonvalved segments and across valve sites (Fig. 6*B*). These values differed significantly, with an average increase of ~2 $cmH_2O$ in valved tracts, reflecting the expected hindrance to flow caused by the intraluminal valve. Results are consistent with data previously reported for rat and mouse lymphatics (33, 46) or in mathematical models (48, 55) and confirm that in this region, valve opening can indeed occur with very low-pressure gradients, well within the capabilities of the less efficient intrinsic contractile activity, typical of diaphragmatic lymphatic vessels.

## Net Lymph Flow in Nonvalved and Valved Vessel Segments

Net lymph flow represents the primary parameter for quantifying the effective hindrance that intraluminal valves impose on lymph propulsion. Relative net lymph progression was significantly greater in valved segments compared with those lacking valves (Fig. 7*A*), leading to a significantly higher net lymph flow in valved segments (Fig. 7*C*). This phenomenon can be explained by the fact that reverse motion of lymph is more pronounced in the absence of an intraluminal valve. Conversely, backward progression is limited even when a valve remains biased open, as indicated by reverse lymph motion through the orifice. The net lymph flow in valved segments (~68% of forward-only flow) is consistent with the "ejection rate" reported for mesenteric lymphatics (45). In contrast, the lower net lymph flow in nonvalved vessel segments (~45.7% of forward-only flow) has not been previously described and may serve as a reference for genetic developmental dysfunctions that impair valve functionality and compromise effective lymph transport (50, 56, 57). Thus, the open-biased state of intraluminal valves remains advantageous compared with the absence of a valve and can sustain effective net lymph progression, at least under intrinsically driven flow in diaphragmatic lymphatics.

Net fractional progression also depended on vessel size, as valved and nonvalved segments of different size displayed divergent trends: valved segments showed increasing distance traveled with larger diameters, whereas nonvalved segments exhibited the opposite behavior (Fig. 7*B*). Overall, the data highlight the pivotal role of intraluminal valves in optimizing net lymph flow, particularly in larger collecting lymphatics. Indeed, net fractional lymph flow appeared independent of vessel size in valved tracts and displayed biphasic behavior in nonvalved segments, with an optimal vessel diameter of ~209 μm, a common value in the diaphragmatic lymphatic network (Fig. 7*D*).

As shown in Fig. 9*A*, net lymph flow was consistently greater in valved segments than in nonvalved tracts, regardless of vessel size (hollow and filled dots, respectively). Nevertheless, this advantage did not result in a statistically significant difference in mean net lymph flow between vessel segments of the two types (Fig. 9*B*), since valved and nonvalved segments alternate along lymphatic collectors and therefore share the same overall net lymph flow.

## Hydraulic Resistance in Nonvalved Segments and across Intraluminal Valves

The calculation of viscous resistance in oscillatory lymph flow requires a precise definition of local flow dynamics. This definition is achieved through computation of both the Reynolds number and the Womersley parameter. In nonvalved segments of elliptical shape, where the diameter ratio is fixed at 0.35, both Reynolds number and Womersley parameter were, as expected, relatively low (~0.026 for Re and 0.029 for $\alpha$). These values indicate laminar flow driven by slow waves generated by intrinsic lymphatic contractions, where viscous forces predominate over inertial ones.

In valved segments, the unknown geometry of the orifice and the funnel-like shape of the valve did not allow for a fixed diameter ratio. A broader scenario was therefore simulated, with a variable diameter ratio of the valve orifice ranging from 1:1 (circular shape, very unlikely given the 3-D reconstructions of valves widely reported in the literature) to 1:0.01, within the limits of other models (51, 53, 58). Results of this simulation are shown in Fig. 10 (hollow dots in Fig. 10, *A* and *B*), indicating that both Re and $\alpha$ remain very low, so that laminar, viscous-dominated flow is also expected for lymph transit through valves.

Based on these premises and following an approach previously used in the literature to address unknown complexities while achieving reliable quantification of resistance (48, 51, 52), "functional" hydraulic resistance was computed by plotting $\Delta P_{lymph}$ as a function of net lymph flow, thereby also accounting for oscillatory intrinsic lymph flow. In this context, the slope of the linear fits in Fig. 11 provided values of "functional" resistance to net lymph flow. In both cases, the slope of the pressure-flow curves was negative, consistent with pump-function curves (48). Quantitatively, the hydraulic resistance values obtained here appear higher than those previously reported in the literature, particularly for mesenteric vessels and numerical simulations (51, 52). This discrepancy may reflect the complexity of the diaphragmatic lymphatic network, which encompasses not only nonlinear mechanics of the vessel wall (59) and intrinsic lymph flow but also the elliptical cross-sectional shape of the vessels, which introduces higher resistance compared with circular conduits due to a greater wetted perimeter-to-area ratio. In addition, hydraulic resistance was measured in several distinct lymphatic vessels, where lymph flow and diameter exhibited concomitant variations. Consequently, a lower flow rate was associated with a smaller vessel, whereas a higher flow rate was associated with a larger vessel (as shown by the primary and secondary *x*-axes in Fig. 11, which depict lymph flow and vessel diameter, respectively). This further illustrates the complexity of the diaphragmatic lymphatic system and highlights that the "functional resistance" reported here inherently captures more of the real physiological complexity and the cumulative hydraulic resistance arising from anatomical and fluid dynamic factors not present in unbranched vessels and often simplified or averaged in computational models.

## Conclusions

Although intraluminal pressure measurements may be marginally influenced by the open ends of the lymphatic network, we minimized this potential artifact by selecting measurement sites located in the central portion of the tissue strip, ensuring that several lymphangions in series separated the recording sites from both open ends. Despite this limitation inherent to the preparation, the data presented in this work highlight the pivotal role of intraluminal valves in shaping intrinsically driven lymph flow in the lymphatic vessels of the diaphragmatic dome. When lymph flow is sustained solely by the intrinsic mechanism, backflow occurs in both nonvalved and valved vessel segments. Although intraluminal valves remain in an open-biased state, a higher $\Delta P_{\mathrm{lymph}}$ is required for lymph progression through valved tracts to overcome the narrowing imposed by the valve. Nevertheless, the presence of intraluminal valves clearly ensures greater net lymph flow compared with nonvalved tracts. Thus, intraluminal valves effectively promote lymph progression even when they remain open-biased, rather than alternating cyclically between open and closed states.

## DATA AVAILABILITY

Data are available upon request to the corresponding author by e-mail at andrea.moriondo@uninsubria.it.

## ACKNOWLEDGMENTS

The authors acknowledge the support of the Applied Research Platform of the Center for Research and Technological Transfer (CRIETT) of the University of Insubria, and its staff, for their assistance in housing and caring for the animal colony used in this study.

## GRANTS

This work has been supported by FAR Grants 2022 and 2023 (to A.M.) from the University of Insubria.

## DISCLOSURES

No conflicts of interest, financial or otherwise, are declared by the authors.

## AUTHOR CONTRIBUTIONS

E.S. and A.M. conceived and designed research; E.S., C.M., and A.M. performed experiments; E.S. analyzed data; E.S., C.M., D.N., and A.M. interpreted results of experiments; E.S. prepared figures; E.S., C.M., and A.M. drafted manuscript; E.S., C.M., D.N., and A.M. edited and revised manuscript; E.S., C.M., D.N., and A.M. approved final version of manuscript.

## REFERENCES

1. **Swartz MA.** The physiology of the lymphatic system. *Adv Drug Deliv Rev* 50: 3–20, 2001. doi:10.1016/s0169-409x(01)00150-8.
2. **Wiig H**, **Swartz MA.** Interstitial fluid and lymph formation and transport: physiological regulation and roles in inflammation and cancer. *Physiol Rev* 92: 1005–1060, 2012. doi:10.1152/physrev.00037.2011.
3. **Solari E**, **Marcozzi C**, **Ottaviani C**, **Negrini D**, **Moriondo A.** Draining the pleural space: lymphatic vessels facing the most challenging task. *Biology (Basel)* 11: 419, 2022. doi:10.3390/biology11030419.
4. **Schmid-Schönbein GW.** Microlymphatics and lymph flow. *Physiol Rev* 70: 987–1028, 1990. doi:10.1152/physrev.1990.70.4.987.
5. **Schmid-Schönbein GW.** The second valve system in lymphatics. *Lymphat Res Biol* 1: 25–29, 2003. doi:10.1089/15396850360495664.
6. **Bazigou E**, **Wilson JT**, **Moore JE Jr.** Primary and secondary lymphatic valve development: molecular, functional and mechanical insights. *Microvasc Res* 96: 38–45, 2014. doi:10.1016/j.mvr.2014.07.008.
7. **Quick CM**, **Venugopal AM**, **Gashev AA**, **Zawieja DC**, **Stewart RH.** Intrinsic pump-conduit behavior of lymphangions. *Am J Physiol Regul Integr Comp Physiol* 292: R1510–R1518, 2007. doi:10.1152/ajpregu.00258.2006.
8. **Muthuchamy M**, **Gashev A**, **Boswell N**, **Dawson N**, **Zawieja D.** Molecular and functional analyses of the contractile apparatus in lymphatic muscle. *FASEB J* 17: 920–922, 2003. doi:10.1096/fj.02-0626fje.
9. **Bridenbaugh EA**, **Gashev AA**, **Zawieja DC.** Lymphatic muscle: a review of contractile function. *Lymphat Res Biol* 1: 147–158, 2003. doi:10.1089/153968503321642633.
10. **Davis MJ**, **Zawieja SD**, **Yang Y.** Developmental progression of lymphatic valve morphology and function. *Front Cell Dev Biol* 12: 1331291, 2024. doi:10.3389/fcell.2024.1331291.
11. **Zawieja DC.** Contractile physiology of lymphatics. *Lymphat Res Biol* 7: 87–96, 2009. doi:10.1089/lrb.2009.0007.
12. **Zawieja DC**, **Davis KL**, **Schuster R**, **Hinds WM**, **Granger HJ.** Distribution, propagation, and coordination of contractile activity in lymphatics. *Am J Physiol Heart Circ Physiol* 264: H1283–H1291, 1993. doi:10.1152/ajpheart.1993.264.4.H1283.
13. **von der Weid P-Y**, **Rahman M**, **Imtiaz MS**, **van Helden DF.** Spontaneous transient depolarizations in lymphatic vessels of the guinea pig mesentery: pharmacology and implication for spontaneous contractility. *Am J Physiol Heart Circ Physiol* 295: H1989–H2000, 2008. doi:10.1152/ajpheart.00007.2008.
14. **Davis MJ**, **Zawieja SD.** Pacemaking in the lymphatic system (Preprint). *J Physiol* 2024. doi:10.1113/JP284752.
15. **Negrini D**, **Marcozzi C**, **Solari E**, **Bossi E**, **Cinquetti R**, **Reguzzoni M**, **Moriondo A.** Hyperpolarization-activated cyclic nucleotide-gated channels in peripheral diaphragmatic lymphatics. *Am J Physiol Heart Circ Physiol* 311: H892–H903, 2016. doi:10.1152/ajpheart.00193.2016.
16. **Russell PS**, **Hong J**, **Trevaskis NL**, **Windsor JA**, **Martin ND**, **Phillips ARJ.** Lymphatic contractile function: a comprehensive review of drug effects and potential clinical application. *Cardiovasc Res* 118: 2437–2457, 2022. doi:10.1093/cvr/cvab279.
17. **Solari E**, **Marcozzi C**, **Negrini D**, **Moriondo A.** Temperature-dependent modulation of regional lymphatic contraction frequency and flow. *Am J Physiol Heart Circ Physiol* 313: H879–H889, 2017. doi:10.1152/ajpheart.00267.2017.
18. **Solari E**, **Marcozzi C**, **Bistoletti M**, **Baj A**, **Giaroni C**, **Negrini D**, **Moriondo A.** TRPV4 channels' dominant role in the temperature modulation of intrinsic contractility and lymph flow of rat diaphragmatic lymphatics. *Am J Physiol Heart Circ Physiol* 319: H507–H518, 2020. doi:10.1152/ajpheart.00175.2020.
19. **Solari E**, **Marcozzi C**, **Negrini D**, **Moriondo A.** Fluid osmolarity acutely and differentially modulates lymphatic vessels intrinsic contractions and lymph flow. *Front Physiol* 9: 871, 2018. doi:10.3389/fphys.2018.00871.
20. **Gashev AA**, **Davis MJ**, **Delp MD**, **Zawieja DC.** Regional variations of contractile activity in isolated rat lymphatics. *Microcirculation* 11: 477–492, 2004. doi:10.1080/10739680490476033.
21. **McHale NG**, **Roddie IC.** The effect of transmural pressure on pumping activity in isolated bovine lymphatic vessels. *J Physiol* 261: 255–269, 1976. doi:10.1113/jphysiol.1976.sp011557.
22. **Telinius N**, **Baandrup U**, **Rumessen J**, **Pilegaard H**, **Hjortdal V**, **Aalkjaer C**, **Boedtkjer DB.** The human thoracic duct is functionally innervated by adrenergic nerves. *Am J Physiol Heart Circ Physiol* 306: H206–H213, 2014. doi:10.1152/ajpheart.00517.2013.
23. **Bachmann SB**, **Gsponer D**, **Montoya-Zegarra JA**, **Schneider M**, **Scholkmann F**, **Tacconi C**, **Noerrelykke SF**, **Proulx ST**, **Detmar M.** A distinct role of the autonomic nervous system in modulating the function of lymphatic vessels under physiological and tumor-draining conditions. *Cell Rep* 27: 3305–3314.e13, 2019. doi:10.1016/j.celrep.2019.05.050.

24. **Scallan JP**, **Zawieja SD**, **Castorena-Gonzalez JA**, **Davis MJ.** Lymphatic pumping: mechanics, mechanisms and malfunction. *J Physiol* 594: 5749–5768, 2016. doi:10.1113/JP272088.
25. **Solari E**, **Marcozzi C**, **Bartolini B**, **Viola M**, **Negrini D**, **Moriondo A.** Acute exposure of collecting lymphatic vessels to low-density lipoproteins increases both contraction frequency and lymph flow: an in vivo mechanical insight. *Lymphat Res Biol* 18: 146–155, 2020. doi:10.1089/lrb.2019.0040.
26. **Solari E**, **Marcozzi C**, **Negrini D**, **Moriondo A.** Lymphatic vessels and their surroundings: how local physical factors affect lymph flow. *Biology (Basel)* 9: 463, 2020. doi:10.3390/biology9120463.
27. **Negrini D**, **Moriondo A.** Lymphatic anatomy and biomechanics. *J Physiol* 589: 2927–2934, 2011. doi:10.1113/jphysiol.2011.206672.
28. **Hynes RO.** The extracellular matrix: not just pretty fibrils. *Science* 326: 1216–1219, 2009. doi:10.1126/science.1176009.
29. **Moriondo A**, **Solari E**, **Marcozzi C**, **Negrini D.** Lymph flow pattern in pleural diaphragmatic lymphatics during intrinsic and extrinsic isotonic contraction. *Am J Physiol Heart Circ Physiol* 310: H60–H70, 2016. doi:10.1152/ajpheart.00640.2015.
30. **Zweifach BW**, **Prather JW.** Micromanipulation of pressure in terminal lymphatics in the mesentery. *Am J Physiol* 228: 1326–1335, 1975. doi:10.1152/ajplegacy.1975.228.5.1326.
31. **Bridenbaugh EA**, **Nizamutdinova IT**, **Jupiter D**, **Nagai T**, **Thangaswamy S**, **Chatterjee V**, **Gashev AA.** Lymphatic muscle cells in rat mesenteric lymphatic vessels of various ages. *Lymphat Res Biol* 11: 35–42, 2013. doi:10.1089/lrb.2012.0025.
32. **Bazigou E**, **Makinen T.** Flow control in our vessels: vascular valves make sure there is no way back. *Cell Mol Life Sci* 70: 1055–1066, 2013. doi:10.1007/s00018-012-1110-6.
33. **Davis MJ**, **Rahbar E**, **Gashev AA**, **Zawieja DC**, **Moore JEJ.** Determinants of valve gating in collecting lymphatic vessels from rat mesentery. *Am J Physiol Heart Circ Physiol* 301: H48–H60, 2011. doi:10.1152/ajpheart.00133.2011.
34. **Blatter C**, **Meijer EFJ**, **Padera TP**, **Vakoc BJ.** Simultaneous measurements of lymphatic vessel contraction, flow and valve dynamics in multiple lymphangions using optical coherence tomography. *J Biophotonics* 11: e201700017, 2018. doi:10.1002/jbio.201700017.
35. **Zawieja SD**, **Castorena-Gonzalez JA**, **Scallan JP**, **Davis MJ.** Differences in L-type $Ca^{2+}$ channel activity partially underlie the regional dichotomy in pumping behavior by murine peripheral and visceral lymphatic vessels. *Am J Physiol Heart Circ Physiol* 314: H991–H1010, 2018. doi:10.1152/ajpheart.00499.2017.
36. **Wolf KT**, **Poorghani A**, **Dixon JB**, **Alexeev A.** Effect of valve spacing on peristaltic pumping. *Bioinspir Biomim* 18: 035002, 2023. doi:10.1088/1748-3190/acbe85.
37. **Bohlen HG**, **Gasheva OY**, **Zawieja DC.** Nitric oxide formation by lymphatic bulb and valves is a major regulatory component of lymphatic pumping. *Am J Physiol Heart Circ Physiol* 301: H1897–H1906, 2011. doi:10.1152/ajpheart.00260.2011.
38. **Wilson JT**, **Wang W**, **Hellerstedt AH**, **Zawieja DC**, **Moore JE.** Confocal image-based computational modeling of nitric oxide transport in a rat mesenteric lymphatic vessel. *J Biomech Eng* 135: 51005, 2013 [Erratum in *J Biomech Eng* 135, 2013]. doi:10.1115/1.4023986.
39. **Moriondo A**, **Bianchin F**, **Marcozzi C**, **Negrini D.** Kinetics of fluid flux in the rat diaphragmatic submesothelial lymphatic lacunae. *Am J Physiol Heart Circ Physiol* 295: H1182–H1190, 2008. doi:10.1152/ajpheart.00369.2008.
40. **Fischer MJM**, **Uchida S**, **Messlinger K.** Measurement of meningeal blood vessel diameter in vivo with a plug-in for ImageJ. *Microvasc Res* 80: 258–266, 2010. doi:10.1016/j.mvr.2010.04.004.
41. **Schneider CA**, **Rasband WS**, **Eliceiri KW.** NIH Image to ImageJ: 25 years of image analysis. *Nat Methods* 9: 671–675, 2012. doi:10.1038/nmeth.2089.
42. **Moriondo A**, **Solari E**, **Marcozzi C**, **Negrini D.** Spontaneous activity in peripheral diaphragmatic lymphatic loops. *Am J Physiol Heart Circ Physiol* 305: H987–H995, 2013. doi:10.1152/ajpheart.00418.2013.
43. **Thévenaz P**, **Unser M.** User-friendly semiautomated assembly of accurate image mosaics in microscopy. *Microsc Res Tech* 70: 135–146, 2007. doi:10.1002/jemt.20393.
44. **Rahbar E**, **Moore JEJ.** A model of a radially expanding and contracting lymphangion. *J Biomech* 44: 1001–1007, 2011. doi:10.1016/j.jbiomech.2011.02.018.
45. **Dixon JB**, **Greiner ST**, **Gashev AA**, **Cote GL**, **Moore JE**, **Zawieja DC.** Lymph flow, shear stress, and lymphocyte velocity in rat mesenteric prenodal lymphatics. *Microcirculation* 13: 597–610, 2006. doi:10.1080/10739680600893909.
46. **Davis MJ**, **Castorena-Gonzalez JA**, **Li M**, **Zawieja SD**, **Simon AM**, **Geng X**, **Srinivasan RS.** Connexin-45 is expressed in mouse lymphatic endothelium and required for lymphatic valve function. *JCI Insight* 9: e169931, 2024. doi:10.1172/jci.insight.169931.
47. **Solari E**, **Marcozzi C**, **Negrini D**, **Moriondo A.** Fluid osmolarity modulates the rate of spontaneous contraction of lymphatic vessels and lymph flow by means of a cooperation between TRPV and VRAC channels. *Biology (Basel)* 12: 1039, 2023. doi:10.3390/biology12071039.
48. **Elich H**, **Barrett A**, **Shankar V**, **Fogelson AL.** Pump efficacy in a two-dimensional, fluid-structure interaction model of a chain of contracting lymphangions. *Biomech Model Mechanobiol* 20: 1941–1968, 2021. doi:10.1007/s10237-021-01486-w.
49. **Li H**, **Mei Y**, **Maimon N**, **Padera TP**, **Baish JW**, **Munn LL.** The effects of valve leaflet mechanics on lymphatic pumping assessed using numerical simulations. *Sci Rep* 9: 10649, 2019. doi:10.1038/s41598-019-46669-9.
50. **Pujari A**, **Smith AF**, **Hall JD**, **Mei P**, **Chau K**, **Nguyen DT**, **Sweet DT**, **Jiménez JM.** Lymphatic valves separate lymph flow into a central stream and a slow-moving peri-valvular milieu. *J Biomech Eng* 142: 100805, 2020. doi:10.1115/1.4048028.
51. **Wilson JT**, **van Loon R**, **Wang W**, **Zawieja DC**, **Moore JEJ.** Determining the combined effect of the lymphatic valve leaflets and sinus on resistance to forward flow. *J Biomech* 48: 3584–3590, 2015. doi:10.1016/j.jbiomech.2015.07.045.
52. **Wilson JT**, **Edgar LT**, **Prabhakar S**, **Horner M**, **van Loon R**, **Moore JEJ.** A fully coupled fluid-structure interaction model of the secondary lymphatic valve. *Comput Methods Biomech Biomed Engin* 21: 813–823, 2018. doi:10.1080/10255842.2018.1521964.
53. **Bertram CD.** Modelling secondary lymphatic valves with a flexible vessel wall: how geometry and material properties combine to provide function. *Biomech Model Mechanobiol* 19: 2081–2098, 2020. doi:10.1007/s10237-020-01325-4.
54. **Moriondo A**, **Solari E**, **Marcozzi C**, **Negrini D.** Diaphragmatic lymphatic vessel behavior during local skeletal muscle contraction. *Am J Physiol Heart Circ Physiol* 308: H193–H205, 2015. doi:10.1152/ajpheart.00701.2014.
55. **Contarino C**, **Toro EF.** A one-dimensional mathematical model of collecting lymphatics coupled with an electro-fluid-mechanical contraction model and valve dynamics. *Biomech Model Mechanobiol* 17: 1687–1714, 2018. doi:10.1007/s10237-018-1050-7.
56. **Castorena-Gonzalez JA**, **Srinivasan RS**, **King PD**, **Simon AM**, **Davis MJ.** Simplified method to quantify valve back-leak uncovers severe mesenteric lymphatic valve dysfunction in mice deficient in connexins 43 and 37. *J Physiol* 598: 2297–2310, 2020. doi:10.1113/JP279472.
57. **Castorena-Gonzalez JA.** Lymphatic valve dysfunction in western diet-fed mice: new insights into obesity-induced lymphedema. *Front Pharmacol* 13: 823266, 2022. doi:10.3389/fphar.2022.823266.
58. **Bertram CD**, **Davis MJ.** An enhanced 3D model of intravascular lymphatic valves to assess leaflet apposition and transvalvular differences in wall distensibility. *Biology (Basel)* 12: 379, 2023. doi:10.3390/biology12030379.
59. **Moriondo A**, **Boschetti F**, **Bianchin F**, **Lattanzio S**, **Marcozzi C**, **Negrini D.** Tissue contribution to the mechanical features of diaphragmatic initial lymphatics. *J Physiol* 588: 3957–3969, 2010. doi:10.1113/jphysiol.2010.196204.